Available online at www.sciencedirect.com
ScienceDirect
Procedia Computer Science 1 (2010) 781–790
Procedia Computer Science
www.elsevier.com/locate/procedia

International Conference on Computational Science, ICCS 2010

Application of the numerical density-enthalpy method to the multi-phase flow through a porous medium

Ibrahim*, [1], F.J.Vermolen*,[2], C.Vuik*,[3]

Faculty EEMCS, Delft Institute of Applied Mathematics, Delft University of Technology, Mekelweg 4, 2628 CD, Delft, The Netherlands

Abstract

In this paper we apply a new method to solve multi-phase fluid flow problem for $1D$ and $2D$ fluid systems. This method is developed at TNO and presented in [1] for spatially homogeneous systems. We call this method the numerical density-enthalpy method (or ρ-h method) because density-enthalpy phase diagrams (or ρ-h diagrams) play an important role in it. Finite elements are used for spatial discretization along with the streamline upwind Petrov-Galerkin method. In contrast to conventional methods, the ρ-h method eliminates the requirement of separate sets of equations for various phases and necessitates fewer parametric assumptions. Therefore, it is aimed at a simple formulation and at an increase of efficiency. © 2010 Published by Elsevier Ltd.

Keywords: multi-phase, porous medium, finite elements, density-enthalpy phase diagram

1. Introduction

Physical models for multi-phase fluid systems in porous media have applications in industrial processes such as drying, steam production, and freezing. These models are meant to simulate the processes to enhance the quality of products. Food items, in general, can be considered as a porous medium (bread, potato etc). In the context of the ρ-h method, Arendsen has presented many applications in his work [1, 2, 3] (a boiler system, potato drying etc). Since several types of phases are present, the interface between adjacent phases has to be tracked. The so called moving interface problems or free boundary problems, are typically solved by methods such as the level-set, moving-grid, and the phase-field model [6, 7, 8]. Level-set and moving-grid models use a sharp interface between adjacent phases. In contrast, the phase-field model allows a diffuse region where, for example, the mass density between the two coexisting phases varies smoothly from one phase to the other [7]. In this paper, we present and use a different method, namely the numerical density-enthalpy method. In [1, 2] a comparison is made of the ρ-h method and standard approaches for modeling thermal processes with phase change. It is a common practice to solve the energy or mass

The author is indebted to HEC, Pakistan and NUFFIC, The Netherlands for their financial and logistic support.

*email address: {d.ibrahim, f.j.vermolen, c.vuik}@tudelft.nl

[1]corresponding author, Faculty EEMCS, Delft Institute of Applied Mathematics, Delft University of Technology, Mekelweg 4, 2628 CD, Delft, The Netherlands

[2]Faculty EEMCS, Delft Institute of Applied Mathematics, Delft University of Technology, Mekelweg 4, 2628 CD, Delft, The Netherlands

[3]Faculty EEMCS, Delft Institute of Applied Mathematics, Delft University of Technology, Mekelweg 4, 2628 CD, Delft, The Netherlands

1877-0509 © 2010 Published by Elsevier Ltd.
doi:10.1016/j.procs.2010.04.084

balance equations alone or to assume constant boiling pressure and temperature. Arendsen also explained that only taking the energy or mass balance is valid for a limited range and that their physical basis is incomplete. Furthermore, the assumption of constant ambient pressure and a fixed phase-change temperature profile cannot always be justified [1, 4]. Another drawback of the aforementioned approaches is that they keep track of the phase change boundary, which might take place only for a small time interval as compared to the whole process. Then these methods switch to another set of equations with a change in phase, which might cause numerical instabilities.

1.1. Density-enthalpy phase diagrams

In this paper we use the mass and energy balances together and use density ρ and enthalpy h as our state variables. These coupled partial differential equations are solved by using finite elements, with a Streamline Upwind Petrov-Galerkin approach. A set of ρ-h diagrams is then used to determine temperature T, pressure P, and mass fractions [1]. In Figure 1, three such diagrams are shown for Propane (C_3H_8), where X_G is the gas mass fraction. Each curve is

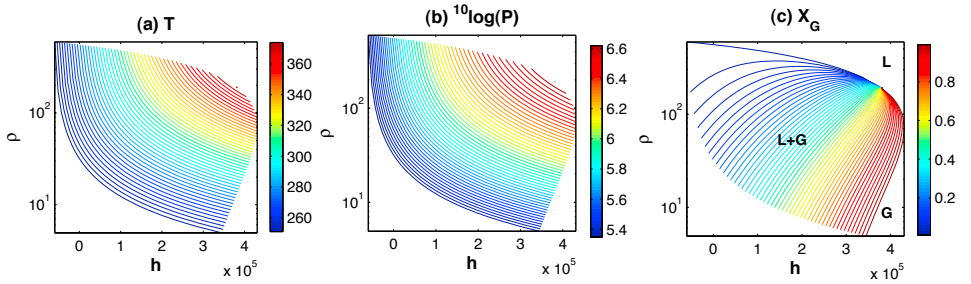

Figure 1: ρ-h diagrams for C_3H_8, (a) Plots of isotherms, (b) isobars, and (c) constant gas mass fraction curves.

obtained through constrained minimization of the total Gibbs free energy as a function of T, P, and mass distribution at given ρ and h [1]. For a given substance (e.g., C_3H_8) we have a unique set of ρ-h diagrams. These diagrams work in a similar way as lookup tables (in the solution algorithm), where ρ and h act as row and column, respectively, whereas the curve color serves as the the table entry for the corresponding variable (i.e., P, T, or X_G). In Figure 1(c), liquid and gas phases are labeled as 'L' and 'G' respectively. The transitional zone is marked with '$L + G$' which is noticeably larger than the 'L' and 'G' zones. Other sets of phase diagrams are also available, which provide, for example, a transformation from (T, X_G) to (ρ, h, and P). In Section 4, numerical results are given as obtained by solving the mass and energy balances for ρ and h and computing P, T, and X_G from ρ-h diagrams. The obtained results are explained qualitatively on the basis of physical laws. This method does not require a constant ambient pressure or a constant phase change temperature. In our view, the ρ-h method is potentially a better approach to model multi-phase fluid systems. Furthermore, it is a multiphysics system in the sense that thermodynamics is considered alongside convection and diffusion aspects in a porous medium. The multiscale aspect is mentioned in Section 5.

2. Problem Definition

We consider the flow of propane (C_3H_8) in a unit square (porous medium) where the interior is represented by Ω and the boundary is designated by Γ. The mathematical model for the two-dimensional system is given by the following partial differential equations.

$$\frac{\partial \rho}{\partial t} + \nabla \cdot (\rho \mathbf{v}) = 0, \qquad \mathbf{x} \in \Omega, \quad t > 0, \text{ (mass conservation)}, \tag{1}$$

$$\frac{\partial (\rho h)}{\partial t} + \nabla \cdot (\rho h \mathbf{v}) = \nabla \cdot (\lambda \nabla T) + q, \qquad \mathbf{x} \in \Omega, \quad t > 0, \text{ (energy conservation)}, \tag{2}$$

$$\mathbf{v} = -\frac{K}{\mu} \nabla P, \qquad \text{(Darcy's Law)}. \tag{3}$$

where the permeability K, dynamic viscosity μ, and heat diffusivity λ are assumed to be constants and q is a heat source. We neglected gravitational effects. Density (ρ) and enthalpy (h) are taken as state variables. Other variables such as temperature (T), pressure (P), and gas mass fraction (X_G) are computed by using ρ-h diagrams. Initial conditions are given by

$$\rho(\mathbf{x}, 0) = \rho_0 \qquad \mathbf{x} \in \Omega, \tag{4}$$

$$h(\mathbf{x}, 0) = h_0 \qquad \mathbf{x} \in \Omega. \tag{5}$$

From a practical point of view, it is more convenient to have initial conditions in terms of T and X_G. Initial conditions for other variables (ρ, h, and P) can be computed from them through phase diagrams. Furthermore, we use Robin boundary conditions. The external mass transfer is proportional to the difference in the internal density (ρ) and the ambient density (ρ_a),

$$\rho\mathbf{v} \cdot \mathbf{n} = k_m(\rho - \rho_a), \quad t > 0, \quad \mathbf{x} \in \Gamma, \tag{6}$$

where k_m is a mass transfer coefficient and $\mathbf{n}$ is an outward unit vector normal to Γ. Equation (6) is the boundary condition for the mass equation. The energy transport across the boundaries takes place if there is a difference in temperature or a difference in density, across boundaries,

$$-\lambda\boldsymbol{\nabla}T \cdot \mathbf{n} + (\rho h)\mathbf{v} \cdot \mathbf{n} = k_h(T - T_a) + h_a k_m(\rho - \rho_a), \qquad t > 0, \quad \mathbf{x} \in \Gamma. \tag{7}$$

where k_h is a heat transfer coefficient.

3. Method description

We solve equations (1) and (2) for ρ and h. The ρ-h diagrams are then used to determine T, P, and X_G. Once the pressure P is obtained, equation (3) is used to find v. To solve the fluid system with finite elements, we start with the standard Galerkin algorithm. Later on the streamline upwind Patrove-Galerkin part of the solution procedure is added.

3.1. Discretization of the mass equation with standard Galerkin approach

In order to get the weak formulation, we discretize equation (1) in time (the Euler backward scheme), multiply it by a test function $\eta(\mathbf{x})$, and integrate over Ω

$$\int_\Omega \frac{\rho^\tau - \rho^{\tau-1}}{\Delta t}\eta d\Omega = -\int_\Omega \boldsymbol{\nabla} \cdot (\rho^\tau \mathbf{v}^{\tau-1})\eta d\Omega, \quad 1 \le \tau \le \tau_{max}, \tag{8}$$

where τ is a time index. Note that the velocity $\mathbf{v}$ is taken at the previous time step $\tau - 1$. The number of time iterations τ_{max} depends on the value of the time step (Δt) between successive iterations. The choice of Δt is discussed later. Now using a vector product rule $\boldsymbol{\nabla} \cdot (\rho\mathbf{v}\eta) = \eta\boldsymbol{\nabla} \cdot (\rho\mathbf{v}) + \rho\mathbf{v} \cdot \boldsymbol{\nabla}\eta$, and the divergence theorem $\int_\Omega \boldsymbol{\nabla} \cdot \mathbf{F} d\Omega = \int_\Gamma \mathbf{F} \cdot \mathbf{n} d\Gamma$, in equation (8) we have

$$\int_\Omega \frac{\rho^\tau - \rho^{\tau-1}}{\Delta t}\eta d\Omega = -\int_\Gamma \rho^\tau \eta \mathbf{v}^{\tau-1} \cdot \mathbf{n} d\Gamma + \int_\Omega \rho^\tau \mathbf{v}^{\tau-1} \cdot \boldsymbol{\nabla}\eta d\Omega. \tag{9}$$

We choose a set of basis functions $\{\phi_i(\mathbf{x})\}_{1 \le i \le N_d}$, where N_d, is the number of mesh nodes for unknowns. The solution is approximated by $\rho^\tau(\mathbf{x}) = \sum_{j=1}^{N_d} \rho_j^\tau \phi_j(\mathbf{x})$. After substitution in the weak form, and choosing $\eta(\mathbf{x}) = \phi_i$, for $i = 1, ..., N_d$, we obtain

$$\sum_{j=1}^{N_d} \frac{\rho_j^\tau - \rho^{\tau-1}}{\Delta t}\left(\int_\Omega \phi_i \phi_j d\Omega\right) = I_1 + \sum_{j=1}^{N_d}\left(\int_\Omega \phi_j \mathbf{v}^{\tau-1} \cdot \boldsymbol{\nabla}\phi_i d\Omega\right)\rho_j^\tau, \tag{10}$$

where I_1 incorporates boundary conditions for an inward velocity, i.e.,

$$I_1 = \begin{cases} -\sum_{j=1}^{N_d}\left(\int_\Gamma k_m \phi_i \phi_j d\Gamma\right)\rho_j^\tau + \int_\Gamma k_m \phi_i \rho_a d\Gamma & \text{if } \mathbf{v}_i^{\tau-1} \cdot \mathbf{n} < 0, \\ -\sum_{j=1}^{N_d}\left(\int_\Gamma \phi_i \phi_j \mathbf{v}^{\tau-1} \cdot \mathbf{n} d\Gamma\right)\rho_j^\tau & \text{if } \mathbf{v}_i^{\tau-1} \cdot \mathbf{n} \ge 0. \end{cases} \tag{11}$$

The problem domain is discretized by using bilinear elements [10]. This gives a system of difference equations of the form

$$M\frac{\boldsymbol{\rho}^{\tau}-\boldsymbol{\rho}^{\tau-1}}{\Delta t}=S_1^{\tau-1}\boldsymbol{\rho}^{\tau}+\mathbf{f}_1^{\tau-1}, \tag{12}$$

where the mass matrix $M=\{M_{ij}\}$, for $i,j\in\{1,...,N_d\}$, is given by

$$M_{ij}=\int_{\Omega}\phi_i\phi_j d\Omega, \tag{13}$$

and the stiffness matrix $S_1^{\tau-1}=\{S_{1_{ij}}^{\tau-1}\}$, for $i,j\in\{1,...,N_d\}$, is

$$S_{1_{ij}}^{\tau-1}=\int_{\Omega}\phi_j\mathbf{v}^{\tau-1}\cdot\boldsymbol{\nabla}\phi_i d\Omega+I_2. \tag{14}$$

The integral I_2 includes boundary conditions for an inwards velocity.

$$I_{2_{ij}}=\begin{cases}-\int_{\Gamma}k_m\phi_i\phi_j d\Gamma, & \text{if } \mathbf{v}_i^{\tau-1}\cdot\mathbf{n}<0,\quad i,j=1,2,\\ -\int_{\Gamma}\phi_i\phi_j\mathbf{v}^{\tau-1}\cdot\mathbf{n}d\Gamma, & \text{if } \mathbf{v}_i^{\tau-1}\cdot\mathbf{n}\geq 0.\end{cases} \tag{15}$$

The vector $\mathbf{f}_1^{\tau-1}=\{\mathbf{f}_{1_i}^{\tau-1}\}$, for $i\in\{1,...,N_d\}$, is

$$\mathbf{f}_1^{\tau-1}=\begin{cases}\int_{\Gamma}k_m\phi_i\rho_a d\Gamma, & \text{if } \mathbf{v}_i^{\tau-1}\cdot\mathbf{n}<0,\\ 0, & \text{if } \mathbf{v}_i^{\tau-1}\cdot\mathbf{n}\geq 0.\end{cases} \tag{16}$$

Global matrices $[M]_{N_d\times N_d}$ and $[S_1]_{N_d\times N_d}$ and the vector $[\mathbf{f}_1]_{N_d\times 1}$ are easier to determine through their respective element matrices (and element vector). For the assembly procedure from element matrices to global matrices, we refer to [10].

3.1.1. Computation of element matrices

By using equation (13), we can determine the element mass matrix for the kth element e_k, $k=1,2,..,N_e$ (N_e= number of elements, whereas N_d is the number of node points)

$$M_{e_{ij}}=\delta_{ij}\frac{\Delta_k}{4}\quad,\ i,j=1,2,3,4, \tag{17}$$

where δ_{ij} represents the Kronecker delta and Δ_k is the area of the kth element. In this paper we use the following Newton-Cotes quadrature rule (for a rectangle)

$$\int_{e_k}I(x,y)dxdy\approx\frac{1}{4}\sum_{i=1}^{4}I(x_i,y_i). \tag{18}$$

where $\{(x_i,y_i),\ i=1,2,3,4\}$ are the corner points of an individual element e_k. In this case, the use of a higher order quadrature rule (e.g., Gaussian quadrature) does not decrease the order of the error because the accuracy is already determined by the nature of the currently used bilinear basis functions for the spatial discretiaztion. The stiffness matrix S_1 is assembled from 2 element matrices, S_{Ω_e} and I_{3_e}. The matrix $[S_{\Omega_e}]_{4\times 4}$ is related to inner rectangular elements whereas $[I_{3_e}]_{2\times 2}$ takes care of boundary elements (line segments). We compute them by using equation (14) and (15)

$$S_{\Omega_{e_{ij}}}=(\boldsymbol{\nabla}_j\phi_i\cdot\mathbf{v}_j^{\tau-1})\frac{\Delta_k}{4}, \qquad i,j=1,2,3,4, \tag{19}$$

$$I_{3_{ij}}=\begin{cases}\delta_{ij}\frac{L}{2}\mathbf{v}_i^{\tau-1}\cdot\mathbf{n} & \text{if } \mathbf{v}_i^{\tau-1}\cdot\mathbf{n}\geq 0,\\ -\delta_{ij}k_m\frac{L}{2} & \text{if } \mathbf{v}_i^{\tau-1}\cdot\mathbf{n}<0,\end{cases} \qquad i,j=1,2, \tag{20}$$

where L is the length of a boundary element. Using equation (16) to compute $\mathbf{f}_{1_e}^{\tau-1}$ for each element at Γ

$$f_{1_{e_i}}=\begin{cases}0 & \text{if } \mathbf{v}_i\cdot\mathbf{n}\geq 0,\\ k_m\rho_a\frac{L}{2} & \text{if } \mathbf{v}_i\cdot\mathbf{n}<0,\quad i=1,2.\end{cases} \tag{21}$$

The global vector $\mathbf{f_1}$ is updated after computation of the element vector f_{1_e}.

3.2. Discretization of the energy equation with standard Galerkin approach

We take $s = \rho h$ and follow a similar procedure as carried out for the mass equation. The time discretized form of equation (2) is given by

$$\frac{s^\tau - s^{\tau-1}}{\Delta t} = \nabla \cdot (s^\tau \mathbf{v}^{\tau-1}) + \nabla \cdot (\lambda \nabla T^{\tau-1}) + q^\tau, \tag{22}$$

where $\mathbf{v}$ and T are taken at the previous time step $\tau - 1$. The weak form is given by

$$\int_\Omega \frac{s^\tau - s^{\tau-1}}{\Delta t}\eta d\Omega = -\int_\Omega \nabla \cdot (s^\tau \mathbf{v}^{\tau-1})\eta d\Omega + \int_\Omega \nabla \cdot (\lambda \nabla T^{\tau-1})\eta d\Omega + \int_\Omega q^\tau \eta d\eta. \tag{23}$$

Substituting

$$\int_\Omega \nabla \cdot (s\mathbf{v})\eta d\Omega = -\int_\Gamma s\eta \mathbf{v} \cdot \mathbf{n} d\Gamma + \int_\Omega s\mathbf{v} \cdot \nabla \eta d\Omega,$$

and

$$\int_\Omega \nabla \cdot (\lambda \nabla T)\eta d\Omega = \int_\Gamma \lambda \frac{\partial T}{\partial n}\eta d\Gamma - \int_\Omega \lambda \nabla T \cdot \nabla \eta d\Omega,$$

into equation (23) we get

$$\int_\Omega \frac{s^\tau - s^{\tau-1}}{\Delta t}\eta d\Omega = -\int_\Gamma s^\tau \eta \mathbf{v}^{\tau-1} \cdot \mathbf{n} d\Gamma + \int_\Omega s^\tau \mathbf{v}^{\tau-1} \cdot \nabla \eta d\Omega + \int_\Gamma \lambda \frac{\partial T^{\tau-1}}{\partial n}\eta d\Gamma - \int_\Omega \lambda \nabla T^{\tau-1} \cdot \nabla \eta d\Omega + \int_\Omega q^\tau \eta d\Omega. \tag{24}$$

Depending on the velocity direction, two boundary integrals in equation (24) can be written as

$$-\int_\Gamma s^\tau \eta \mathbf{v}^{\tau-1} \cdot \mathbf{n} d\Gamma + \int_\Gamma \lambda \frac{\partial T^{\tau-1}}{\partial n}\eta d\Gamma = \begin{cases} -\int_\Gamma h_a k_m (\rho^\tau - \rho_a) d\Gamma - \int_\Gamma k_h (T^{\tau-1} - T_a) d\Gamma, & \mathbf{v} \cdot \mathbf{n} < 0 \\ -\int_\Gamma s^\tau \eta \mathbf{v}^{\tau-1} \cdot \mathbf{n} d\Gamma - \int_\Gamma k_h (T^{\tau-1} - T_a) d\Gamma, & \mathbf{v} \cdot \mathbf{n} \geq 0 \end{cases}$$

The system of difference equations corresponding to equation (24) is given as

$$M \frac{\mathbf{s}^\tau - \mathbf{s}^{\tau-1}}{\Delta t} = S_2^{\tau-1} \mathbf{s}^\tau + \mathbf{f}_2^{\tau-1}, \tag{25}$$

where M is the same as in the previous subsection. The stiffness matrix S_2 is assembled from two element matrices, $S_{\Omega_{e_k}}$ and I_{4_e}. The matrix $[S_{e_k}]_{4\times4}$ is given earlier and $[I_{4_e}]_{2\times2}$ is given as

$$I_{4_{e_{ij}}} = \begin{cases} \delta_{ij} \frac{L}{2} \mathbf{v}_i^{\tau-1} \cdot \mathbf{n} & \text{if } \mathbf{v}_i^{\tau-1} \cdot \mathbf{n} \geq 0, \quad i, j = 1, 2 \\ 0 & \text{if } \mathbf{v}_i^{\tau-1} \cdot \mathbf{n} < 0. \end{cases} \tag{26}$$

The R.H.S. vector $\mathbf{f}_2^{\tau-1}$, for $k \in \{1, ..., N_d\}$ is given by

$$\mathbf{f}_{2_i}^{\tau-1} = -\int_\Gamma k_h (T^{\tau-1} - T_a)\phi_i d\Gamma - \int_\Omega \lambda \nabla T^{\tau-1} \cdot \nabla \phi_i d\Omega + \int_\Omega q^\tau \phi_i d\Omega + I_5, \tag{27}$$

$$I_5 = \begin{cases} 0, & \text{if } \mathbf{v}^{\tau-1} \cdot \mathbf{n} \geq 0, \\ -\int_\Gamma k_m h_a (\rho^\tau - \rho_a) \phi_i d\Gamma, & \text{if } \mathbf{v}^{\tau-1} \cdot \mathbf{n} < 0. \end{cases} \tag{28}$$

In our algorithm, the R.H.S. vector $[\mathbf{f}_2]_{N_d\times1}$ is assembled from two element vectors $[\mathbf{f}_{\Omega_e}]_{4\times1}$ and $[\mathbf{f}_{\Gamma_e}]_{2\times1}$, corresponding to inner elements e_k and boundary elements, respectively.

$$f_{\Omega_{e_i}} = -\int_{e_{xy}} \lambda \nabla T^{\tau-1} \cdot \nabla \phi_i dxdy + \int_{e_{xy}} q^\tau \phi_i dxdy, \quad i = 1, 2, 3, 4 \tag{29}$$

$$= -\sum_{j=1}^{4} \sum_{l=1}^{4} \frac{\lambda}{4} T_k^{\tau-1} \left(\frac{\partial \phi_i}{\partial x_j} \frac{\partial \phi_l}{\partial x_j} + \frac{\partial \phi_i}{\partial y_j} \frac{\partial \phi_l}{\partial y_j} \right) \Delta_k + \frac{1}{4} \sum_{j=1}^{4} q_j^\tau \Delta_k. \tag{30}$$

$$f_{\Gamma_{e_i}} = \begin{cases} I_e & \text{if } \mathbf{v}^{\tau-1} \cdot \mathbf{n} \geq 0, \quad i = 1, 2, \\ -k_m h_a \frac{L}{2}(\rho_i^{\tau} - \rho_a) + I_{e_i} & \text{if } \mathbf{v}^{\tau-1} \cdot \mathbf{n} < 0, \end{cases} \tag{31}$$

where I_e comes from the first integral on the R.H.S. of equation (27) and it is given by

$$\begin{aligned} I_{e_i} &= -\int_{e_\Gamma} k_h (T^{\tau-1} - T_a)\phi_i d\Gamma \\ &= -k_h \frac{L}{2}(T_i^{\tau-1} - T_a). \end{aligned} \tag{32}$$

3.3. Calculation of the velocity from Darcy's law

Once ρ and h have been determined, ρ-h diagrams are used to compute T, P, and X_G. Subsequently, Darcy's law is used to calculate $\mathbf{v}$ from P. To this extent, we use a weak form of Darcy's law, which reads as

$$\int_\Omega v_x \eta d\Omega = -\int_\Omega \frac{K}{\mu}\frac{\partial P}{\partial x}\eta d\Omega, \tag{33}$$

$$\int_\Omega v_y \eta d\Omega = -\int_\Omega \frac{K}{\mu}\frac{\partial P}{\partial y}\eta d\Omega, \tag{34}$$

for both components of the velocity $\mathbf{v}$. We write $v_x(\mathbf{x}) = \sum_{j=1}^{N_d} v_{x_j}\phi_j(\mathbf{x})$, $v_y(\mathbf{x}) = \sum_{j=1}^{N_d} v_{y_j}\phi_j(\mathbf{x})$, and $P(\mathbf{x}) = \sum_{j=1}^{N_d} P_j\phi_j(\mathbf{x})$ to obtain

$$\sum_{j=1}^{N_d} v_{x_j} \int_\Omega \phi_i\phi_j d\Omega = -\sum_{j=1}^{N_d} P_j \int_\Omega \frac{K}{\mu}\frac{\partial \phi_j}{\partial x}\phi_i \, d\Omega, \quad i = 1, 2, ..., N_d, \tag{35}$$

$$\sum_{j=1}^{N_d} v_{y_j} \int_\Omega \phi_i\phi_j d\Omega = -\sum_{j=1}^{N_d} P_j \int_\Omega \frac{K}{\mu}\frac{\partial \phi_j}{\partial y}\phi_i \, d\Omega, \quad i = 1, 2, ..., N_d. \tag{36}$$

Let $m_{ij} = \int_\Omega \phi_i\phi_j d\Omega$, $f_{x_i} = -\int_\Omega \frac{K}{\mu}\frac{\partial}{\partial x}\left(\sum_{j=1}^{N_d} P_j\phi_j\right) d\Omega$, and $f_{y_i} = -\int_\Omega \frac{K}{\mu}\frac{\partial}{\partial y}\left(\sum_{j=1}^{N_d} P_j\phi_j\right) d\Omega$, then these matrices assembled from the following element matrices

$$m_{2_{ij}} = \frac{\Delta_k}{4}\delta_{ij}, \tag{37}$$

$$f_{x_i} = -\frac{\Delta_k}{4}\frac{K}{\mu}\sum_{j=1}^{4} P_j \frac{\partial \phi_j}{\partial x_k}, \tag{38}$$

$$f_{y_i} = -\frac{\Delta_k}{4}\frac{K}{\mu}\sum_{j=1}^{4} P_j \frac{\partial \phi_j}{\partial y_k}. \tag{39}$$

Since $M_2 = [m_{ij}]_{N_d \times N_d}$ is a diagonal matrix, the solution procedure of the system of equations is trivial.

3.4. Streamline Upwind Petrov-Galerkin method

We use this method to avoid numerical oscillations caused by a convection dominant problem. In this method, the test function $\eta(\mathbf{x})$ includes another term $p(\mathbf{x})$ alongside the classical part (say $w(\mathbf{x})$). The classical part ensures consistency of the scheme and $p(\mathbf{x})$ introduces some artificial diffusion (and hence some loss of accuracy). In our case

$$p(\mathbf{x}) = \frac{D}{2}\frac{\mathbf{v} \cdot \boldsymbol{\nabla}\phi_i}{|\mathbf{v}|}, \quad |\mathbf{v}| > 0. \tag{40}$$

The value of D depends on the direction of the velocity and element dimensions [10]. With the modified test function, $\eta(\mathbf{x}) = w(\mathbf{x}) + p(\mathbf{x})$, we need to repeat all the steps carried out in the preceding subsections to determine element and global matrices [10].

Symbol	value	comments/units
K	10^{-10}	$[m^2]$
h_a	3.5×10^4	$[J/Kg]$
Δt	1/16000	(with Δx =0.025)$[s]$
μ	5×10^{-5}	$Pa.s$
λ	0.05	$[W/m/K]$

Table 1: Parametric values.

4. Numerical Experiments

For the simulation results of this section, the $2D$ domain is divided into 40×40 elements (and $1D$ into 40 elements). We assume no heat source ($q = 0$) for the given examples. Few other parameter values are provided in Table 1

4.1. Case Study 1. Inwardly insulated system

We start with a simpler case, where no mass and heat is allowed to enter the fluid system by setting $k_m = k_h = 0$. The model and the solution procedure still allow an outflow of the mass and energy. To ensure a positive initial velocity, we take the following initial conditions

$$T(\mathbf{x}, 0) = 292 - 2x, \qquad \mathbf{x} \in \Omega,$$
$$X_G(\mathbf{x}, 0) = 0.1, \qquad \mathbf{x} \in \Omega,$$

where Ω is a unit length line segment for $1D$ and a unit square for $2D$ model. An exact relation between T and P is not known in the context of the numerical ρ-h method. However, in our case, it is known experimentally (and partially supported by Van der Waals equation), that a linear temperature profile results in an almost linear pressure. The simulation results for all solution variables, ρ, ρh, T, P, X_G, and v ($1D$ case) are given in Figure 2. The $2D$

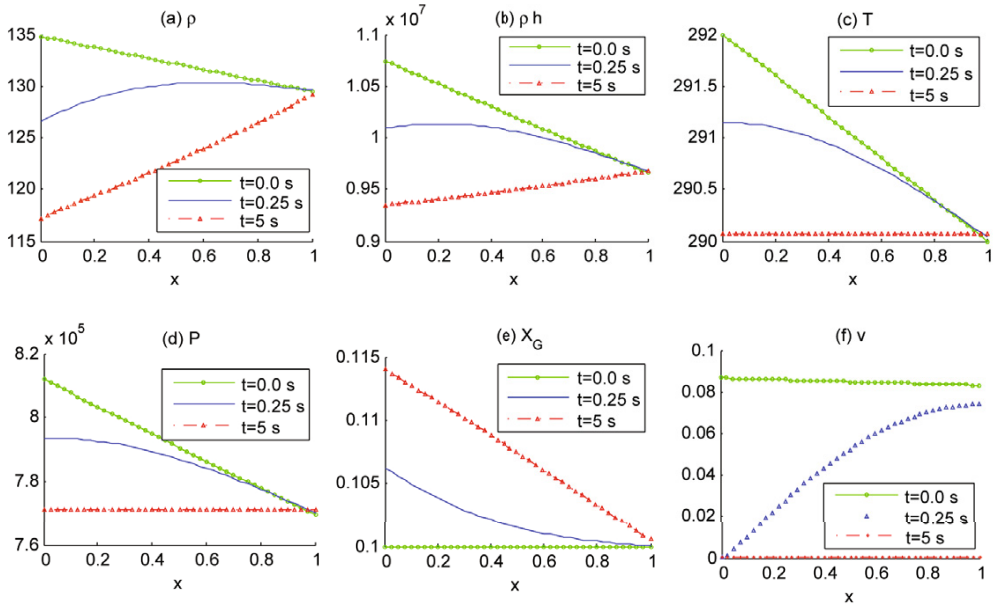

Figure 2: Case Study 1. Inwardly insulated system, ($k_m = 0$, $k_h = 0$). Solution variables at $t = 0,\ 0.25,\ 5.0$ $[s]$, (a) density, (b) total enthalpy ρh, (c) temperature T, (d) pressure P, (e) gas mass fraction X_G, and (f) velocity v.

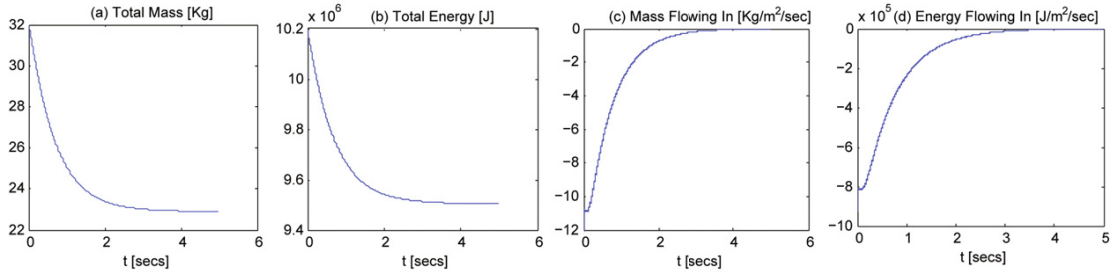

Figure 3: Case Study 1. (a) total mass, (b) total energy, (c) mass flow rate, and (d) energy flow rate.

results are given in Figure 4 and 5 with a similar initial conditions. A higher pressure value in the left part of the domain, as compared to the right part (Figure 2(d)), forces a positive velocity (Figure 2(f)). The mass cannot enter from the left boundary ($k_m = 0$), therefore, the velocity at the left boundary node goes to zero immediately. A positive velocity means that the density in the left side decreases with time (Figure 2(a)). It also means that the mass and the

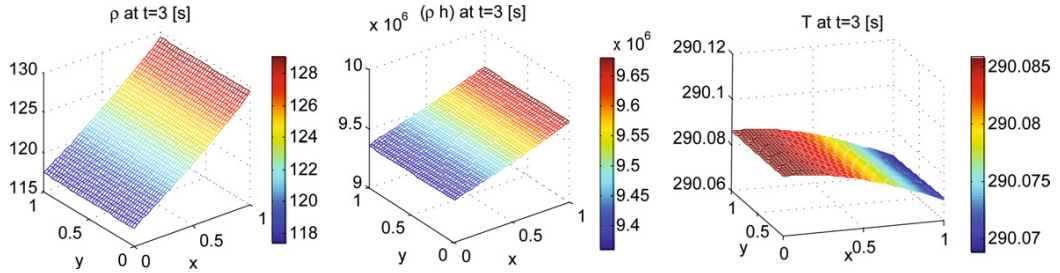

Figure 4: Case Study 1. Inwardly insulated system ($k_m = 0$, $k_h = 0$), $2D$ model with 1D conditions, (left) density ρ, (middle) total enthalpy ρh, and (right) temperature T.

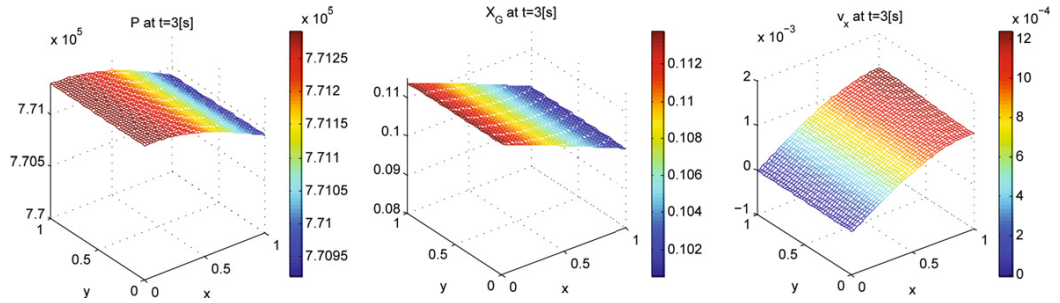

Figure 5: Case Study 1. $2D$ model with 1D conditions. Solution variables at $t = 3.0$ (left) pressure P, (middle) gas mass fraction X_G, and (right) velocity v_x in x-direction.

energy are flowing out from the right boundary. A decreasing density in the left side implies that the gas mass fraction (relative to liquid mass fraction) is increasing in that section (Figure 2(e)). Figure 3(a) shows that the total mass in the fluid system ($\int_\Omega \rho d\Omega$) decreases with time, before reaching to a steady-state value. The total energy ($\int_\Omega \rho h d\Omega$) is also shown in Figure 3(b). The total energy decreases because of the outward mass transportation. The mass and energy flow rates are given by equations (6) and (7) (analytically). For their efficient numerical computation, see [4]. These flow rates (as given in Figure 3(c) and 3(d)) are also used to check for the mass and energy conservation conditions. In accordance with Fourier's law, the temperature (and pressure) decreases in the left part and as the time proceeds

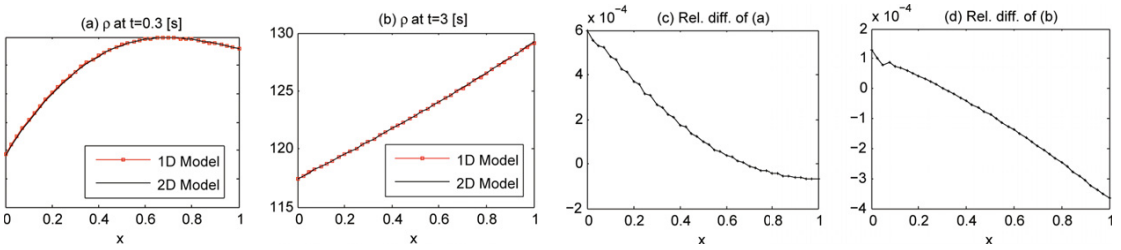

Figure 6: Case 1. Inwardly insulated system ($k_m = 0$, $k_h = 0$), comparison of $1D$ density plots with graphs taken from cross-section of $2D$ plots. (a) density values at $t = 0.3$ $[s]$ (b) density values at $t = 3.0$ $[s]$ (c) the relative difference of two density curves given in (a), i.e., $\frac{(\rho_i^\tau)_{2D}-(\rho_i^\tau)_{1D}}{(\rho_i^\tau)_{2D}}$, $1 \leq i \leq 41$ and (d) the relative difference of two density curves given in (b).

the temperature (and pressure) gradient decreases (Figure 2(c) and 2(d)). A decreasing pressure gradient lowers the magnitude of the velocity. Both, the mass and heat, flow from left to right, therefore, the total enthalpy also decreases in the left part and increases, relatively, in the right side as shown in Figure 2(b). Apart from the comparison of ρ, h, T, and P values in left and right sides, they always decrease in absolute terms due to the mass outflow. The transport of mass and energy continues until the temperature (and pressure) gradient becomes zero. It is obvious that the temperature and pressure are the main drivers for all transport. Other variables (ρ, h, X_G, and v) depend on T and P whereas T and P tend to a steady state. The transfer of mass and heat stops as soon the system reaches its steady state value (thermal equilibrium). A comparison for density graphs of 1- and $2D$ calculations is given in Figure 6, where cross-sections of $2D$ density graphs (along the x-axis) are provided along with $1D$ graphs for given time instances. There is no significant relative difference ($\frac{(\rho_i^\tau)_{2D}-(\rho_i^\tau)_{1D}}{(\rho_i^\tau)_{2D}}$, $1 \leq i \leq 41$) between the two models for this example.

4.2. Case Study 2. Mass and energy flowing into the system

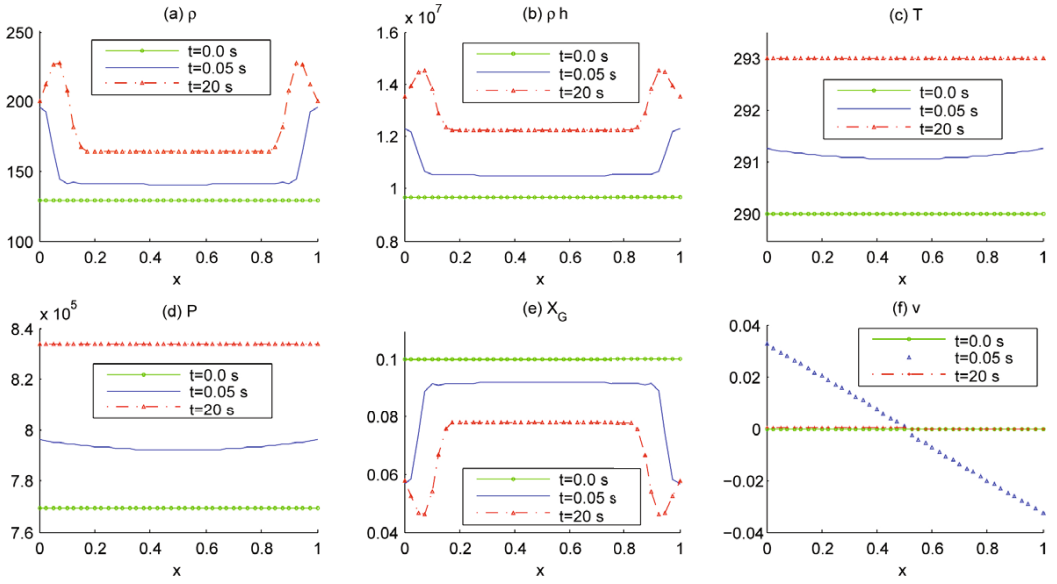

Figure 7: Case Study 2. Mass and energy are flowing into the system, ($k_m = 1.5$, $k_h = 10^5$). Solution variables at $t = 0,\ 2,\ 20$ $[s]$, (a) density, (b) total enthalpy ρh, (c) temperature T, (d) pressure P, (e) gas mass fraction X_G, and (f) velocity v.

In this Case Study, we set initial conditions ($T(x, 0) = 290$ $[K]$, $X_G = 0.1$ $[kg/kg]$) and the ambient temperature

(T_a = 293) for an inward initial velocity and hence an inward transport of mass (k_m = 1.5 $[m/s]$) and heat ($k_h = 10^5$). Simulation results ($1D$ model) are given in Figure 7. Again, the temperature (and pressure combination) is the main driver of the system dynamics. For more explanations, we refer to the subsection for Case Study 1 and [10]. Note that the system (Figure 7) approaches a steady state as soon the temperature T approaches T_a (=293).

5. Conclusions

The numerical ρ-h method can be successfully applied to multi-phase fluid systems where we have certain spatial profiles for the system variables. The solution of $1D$ and $2D$ models leads to comparable results for problems with a $1D$ solution profile. At this moment, the time step Δt should be chosen very small. This leads to excessive amounts of computing times. For this model we do not have an analytic upper bound for Δt in order to obtain a stable time integration. The upperbound is determined experimentally. Currently, we are investigating the origin of the small Δt requirement. In our view, multiple time scales are involved in this model, which makes the resulting system of discretized partial differential equations very stiff. The physical background of the multi time scales are the time-scale of the convection diffusion process and the time-scale of the phase change process. In the future we plan to investigate the cause of the stiffness. Thereafter we consider a fully implicit time integration, an adaptive Δt strategy, and an adaptation of the thermodynamic model in the neighborhood of phase changes in order to reduce the computing times.

References

[1] A. R. J. Arendsen, A. I. van Berkel, A. B. M. Heesink, and G. F. Versteeg. Dynamic modelling of thermal processes with phase transitions by means of a density-enthalpy phase diagram. 7th World Congress of Chemical Engineering, Glasgow, Scotland, 2005.
[2] A. R. J. Arendsen and G. F. Versteeg. Dynamic modelling of refrigeration cycles using density and enthalpy as state variables. 17th International Congress of Chemical and Process Engineering, Prague, The Czech Republic, 2006.
[3] A. R. J. Arendsen and G. F. Versteeg. Dynamic Thermodynamics with Internal Energy, Volume, and Amount of Moles as States: Application to Liquefied Gas Tank. Ind. Eng. Chem. Res. 2009, 48, 3167-3176.
[4] Abdelhaq Abouhafç. Finite Element Modeling Of Thermal Processes With Phase Transitions. Master Thesis, 2007, Delft University of Technology.
[5] Ibrahim, C. Vuik, F.J. Vermolen, D. Hegen. Numerical Methods for Industrial Flow Problems. Delft University of Technology 08-13, 2008.
[6] E. Javierre, C. Vuik, F. J. Vermolen, S. van der Zwaag. A comparison of numerical models for one-dimensional Stefan problems. J. Comp. Appl. Math., 2006, 192, 445-459.
[7] Heike Emmerich. The Diffuse Interface Approach in Materials Science, Thermodynamic Concepts and Applications of Phase-Field Models. Springer, Berlin, 2003.
[8] J.H. Brusche, A. Segal, and C. Vuik. An efficient numerical method for solid-liquid transitions in optical rewritable recording. International Journal for Numerical Methods in Engineering, 77, pp. 702-718, 2009.
[9] O.C. Zienkiewicz, R.L. Taylor, & J.Z. Zhu. The Finite Element Method, Its Basis & Fundamentals. 6e, Butterworth-Heinemann, 2005.
[10] Ibrahim, C. Vuik, F.J. Vermolen, D. Hegen. Numerical Methods for Industrial Flow Problems. Delft University of Technology 09-10, 2009.